Pressure-Driven, Resistive Magnetohydrodynamic Interchange Instabilities in Laser-Produced, High-Energy-Density Plasmas

Introduction

Pressure-driven, resistive interchange modes are fundamental magnetohydrodynamic (MHD) instabilities in plasmas.[1–4] These convective instabilities occur under circumstances with unfavorable field curvature relative to the pressure gradient [$\boldsymbol{\kappa} \bullet \nabla P > 0$, where $\boldsymbol{\kappa} = \mathbf{B} \bullet \nabla \mathbf{B}/B^2$ is the line curvature of the magnetic (B) field and ∇P is the plasma pressure gradient]. In this configuration, field lines are concave toward the plasma and have tension that tends to make them shorten and collapse inward, while plasma pressure has a natural tendency to expand outward. Unstable perturbations that have short wavelengths perpendicular to the B field ($k_{\perp} L_p \gg 1$, where $L_p \equiv P/\nabla P$ is the pressure scale length) and long wavelengths parallel to the field ($k_{||}$) grow and result in interchanges of field and their plasma content between the inside and outside of the plasma edge, leading to a state of lower internal energy. The instabilities evolve through a linear-growth phase, followed by a nonlinear one.[3,4] The basic behavior of these unstable modes is analogous to the Rayleigh–Taylor (RT) instabilities, which are driven by acceleration (equivalent to the pressure gradient for interchange instabilities) in plasmas.[3,4] Interchange instabilities have been widely studied in the magnetically confined, tenuous plasmas[1–4] but have not been explored, to our knowledge, in high-temperature, dense, high-energy-density (HED) plasmas.[5]

Laser-produced plasmas are typical HED plasmas with thermal and/or magnetic pressures >1 Mbar (Ref. 5). Generated by a circular laser beam interacting with a solid foil, a plasma bubble[6–9] is similar to those plasmas confined by a typical Z pinch. Ideal MHD theory,[3] which ignores plasma resistivity, predicts that the only unstable interchange modes are the $m = 0$ (sausage instability) and the $m = 1$ (kink instability), while the other $m > 1$ modes are stabilized because their growth is energetically unfavorable in overcoming the tension generated by the curvature of B-field lines ($\propto B^2/r$), where r is the curvature radius. The stabilizing field-line bending effect can be significantly reduced in resistive plasmas since the plasma resistivity results in field slipping and diffusion across the plasma boundary, making it possible for high-mode-number modes to be destabilized and to grow. This scenario is illustrated schematically in Fig. 118.17.

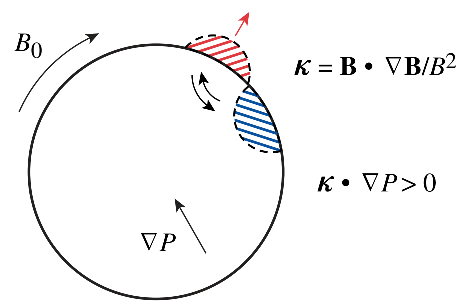

Figure 118.17
Top view (schematic) of a laser-generated plasma bubble, illustrating a high-mode-number ($m > 1$), pressure-driven, resistive MHD interchange instability resulting in an interchange of fields between the inside and outside of the bubble edge. The diffusion of the B field reduces the effect of field-line bending. B_0 represents the undisturbed B field.

The first observation of such an edge asymmetry in laser-produced plasmas by proton radiography of laser–foil interactions was recently reported.[6] Based largely on conceptual arguments and order-of-magnitude estimates, therein it was conjectured that this asymmetric structure was a consequence of pressure-driven, resistive MHD interchange instabilities. This hypothesis is made quantitative and more rigorous in this article. The generation of laser-produced spontaneous magnetic fields is outlined. A theoretical description of the features of interchange modes in HED plasmas is then presented. The theory is supported by experimental results and discussions are presented. The important findings are then summarized.

Laser-Produced, High-Energy-Density Plasmas and Spontaneous Magnetic Fields

Laser-generated plasmas are transient with durations of the order of a few nanoseconds. High plasma densities ($\sim 10^{18}$ cm^{-3}), high temperatures ($\sim$1 keV), intense self-generated B fields [$\sim$1 megagauss (MG)], and high ratios of thermal pressure to magnetic pressure ($\beta \gg 1$) distinguish this from the tenuous plasmas of the order of 10^{14}/cm^3 or lower, which are characteristics of most magnetic-confinement experiments. For long-pulse, low-intensity laser light, the dominant source for B-field generation is noncollinear electron-density and temperature gradients ($\nabla n_e \times \nabla T_e$), where n_e is the electron density and T_e is the temperature.[10–12] In the regime with a low-ionization-state Z and high temperature, where resistivity is low, B-field growth is linear in time and is balanced by convective transport[10–12] [$\nabla \times (\mathbf{v} \times \mathbf{B})$, where $\mathbf{v}$ is the plasma fluid velocity; i.e., the B field is "frozen in"]. When the laser is off and the cooling plasma becomes more resistive, field diffusion dominates convective transport[10–12] [$\nabla \times (D_m \nabla \times \mathbf{B})$, where D_m is the magnetic diffusion coefficient]. Under these circumstances, B-field generation and evolution are governed by[10–12]

$$\frac{\partial \mathbf{B}}{\partial t} \approx \nabla \times (\mathbf{v} \times \mathbf{B}) - \frac{1}{e n_e} \nabla n_e \times \nabla T_e - \nabla \times \left(D_m \nabla \times \mathbf{B}\right), \quad (1)$$

where e is the electron charge.

Figure 118.18 shows the spatial distributions of n_e, T_e, and B field in a plasma bubble caused by the interaction of a laser beam (wavelength = 0.351 nm, 1-ns pulse with a beam-spot size ~800 μm in diameter, and energy ~400 J), with a 5-μm-thick plastic (CH) foil at a time of 1.8 ns, simulated by the two-dimensional (2-D) radiation–hydrodynamics code LASNEX.[13,14] The maximum field strength occurs around the surface of the hemispherical plasma bubble because the largest temperature gradients occur around the bubble's edge. The relative importance of plasma convection to diffusion during field evolution is characterized by the magnetic Reynolds number

$$R_m = \frac{L_\perp \mathbf{v}}{D_m} \approx \left| \frac{\nabla \times (\mathbf{v} \times \mathbf{B})}{\nabla \times \left(D_m \nabla \times \mathbf{B}\right)} \right|, \quad (2)$$

where $L_\perp$ is the characteristic length scale.[3,4] When the laser is on, $R_m \gg 1$; therefore, the fields must be frozen in and move with the plasmas (for example, taking a characteristic scale length $L_\perp \approx T_e / \nabla T_e \sim 100\ \mu$m , a bubble expansion velocity $v \sim 5 \times 10^7$ cm/s, and a diffusion $D_m \sim 4 \times 10^2$ cm^2/s, one has $R_m \sim 1000$). The flow is dominated by plasma fluid dynamics and is insignificantly affected by the fields despite their MG levels.[6–8,15] The bubble expansion in this regime can be approximated as "free-streaming" because the velocity is of the order of the ion sound velocity ($C_s \sim 2 \times 10^7$ cm/s). After the laser pulse turns off (the energy input is stopped), the plasma bubble continues to expand and begins to cool. The cooling plasma becomes more collisional and increasingly resistive. This makes it possible for the field to diffuse across the plasma boundary and eventually dissipate. At these post-driven times, the fluid behavior near the plasma edge is increasingly governed by the field and resistive effects (i.e., $R_m < 1$), and the local plasma β becomes of the order of 1 (Refs. 6–8,15). As will be shown, this gives rise to pressure-driven resistive instabilities. The large amplitudes of unstable modes, resulting from exponential growth around the plasma bubble edge, provide unique opportunities for the experimental study of such important instabilities in HED plasmas.

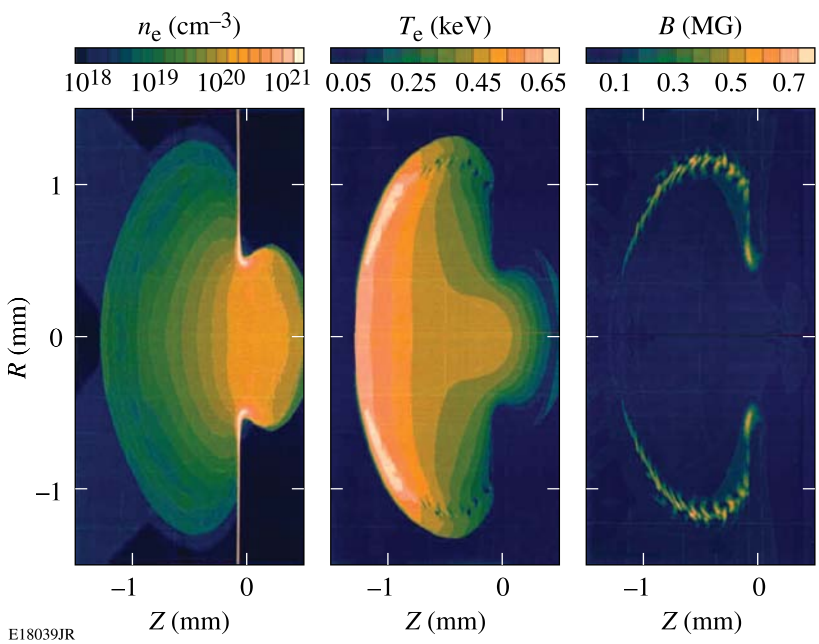

Figure 118.18
Side view of the distributions of n_e, T_e, and B-field amplitude in an isolated laser-generated plasma bubble at t = 1.8 ns for a 1-ns laser drive pulse with a beam-spot size ~800 μm in diameter, simulated with the 2-D code LASNEX. The surface of the foil is at position Z = 0.0 on the horizontal axes, and the laser is incident from the left. The field is always perpendicular to the plane of the image.

Pressure-Driven Resistive Instabilities

In analyzing the instabilities in the linear growth phase, it is assumed that the perturbations are small so that the linearized MHD equations can be used to elucidate the fundamental features of the instabilities. Considering the small-scale modes ($k_\perp L_p \gg 1$), linearizing the equations ($\partial/\partial t \longrightarrow \gamma$, where γ is the growth rate) and Fourier transforming the perturbations ($\nabla \longrightarrow ik$), a set of algebraic high-β-reduced MHD eigen-equations is obtained.[4] By solving for the eigenvalues, a dispersion relation for the mode growth rate is obtained:[4]

$$\gamma^2 \approx \frac{2(\mathbf{B}\cdot\nabla\mathbf{B})\nabla P}{\rho B^2} - \frac{k_\parallel^2 v_A^2}{1 + D_\mathrm{m} k_\perp^2 \gamma^{-1}}. \tag{3}$$

In this dispersion equation, the second term represents the mode stabilization caused by the field-line bending. Perturbations are stabilized when

$$\frac{2(\mathbf{B}\cdot\nabla\mathbf{B})\nabla P}{\rho B^2} \le \frac{k_\parallel^2 v_A^2}{1 + D_\mathrm{m} k_\perp^2 \gamma^{-1}}, \tag{4}$$

where

$$v_\mathrm{A} = \sqrt{\frac{B^2}{\rho}} \tag{5}$$

is the Alfvén speed, and the wave number along the toroidal *B* field is

$$k_\parallel = \frac{m}{2\pi R}, \tag{6}$$

where m is the mode number. As illustrated in Fig. 118.18, the scale length of the temperature is about 30% of the bubble radius (R), i.e., $L_T \sim 0.3 \times R$. The wave number perpendicular to the field line is given as approximately $k_\perp \sim L_B^{-1} \left(L_B \equiv B/\nabla B \sim 0.1 \times R\right)$. Considering $\nabla \sim L_T^{-1}$, the field-line curvature is approximately

$$|\boldsymbol{\kappa}| = \left|\frac{\mathbf{B}\cdot\nabla\mathbf{B}}{B^2}\right| \sim \frac{1}{L_T}. \tag{7}$$

The magnetic diffusion coefficient is

$$D_\mathrm{m} = \frac{c^2}{4\pi}\eta, \tag{8}$$

where η is the plasma resistivity. Using $L_T \sim 0.3\,R$, the dispersion relation [Eq. (3)] can be rewritten as

$$\begin{aligned}\gamma^2 &\sim \frac{2P}{\rho L_T^2} - \frac{m^2 B^2}{\rho(2\pi R)^2\left(1 + D_\mathrm{m} k_\perp^2 \gamma^{-1}\right)} \\ &\sim \frac{2B^2\beta}{\rho\pi R^2} - \frac{m^2 B^2}{4\rho\pi^2 R^2\left(1 + D_\mathrm{m} k_\perp^2 \gamma^{-1}\right)}.\end{aligned} \tag{9}$$

When $\gamma^2 \le 0$, the (minimum) condition for perturbation stabilization caused by the effects of field-line bending becomes

$$\beta - \frac{m^2}{8\pi\left(1 + D_\mathrm{m} k_\perp^2 \gamma_\mathrm{max}^{-1}\right)} \le 0 \tag{10}$$

or

$$m > \sim\sqrt{8\pi\beta\left(1 + D_\mathrm{m} k_\perp^2 \gamma_\mathrm{max}^{-1}\right)}, \tag{11}$$

where

$$\gamma_\mathrm{max} = \gamma\,\big|_{m=0} \tag{12}$$

is the maximum growth rate that occurs when $m = 0$, i.e., sausage instability. As indicated by Eq. (3), the effect of field-line bending on stabilizing perturbations will be significantly reduced when $D_\mathrm{m} k_\perp^2 \gamma^{-1} \ge 1$ (Ref. 4).

When compared to typical tenuous plasmas with low-plasma β's ($\ll 1$), typical laser-produced HED plasmas have, as discussed in the previous section, relatively large plasma β's, allowing a much higher mode-number cutoff for stabilizing perturbations. For physical quantities of experiments relevant to the laser–foil interactions[6–8,15] on OMEGA[16] [taking typical values in the region around the plasma edge after the laser turns off (Fig. 118.18)], $n_i \sim 1 \times 10^{18}$ cm^{-3}, $n_\mathrm{e} \approx Zn_i \sim 3.5 \times 10^{18}$ cm^{-3}, $T_\mathrm{e} \sim 0.4$ keV, $B \sim 0.3$ MG, and $\beta \sim 1$, with an estimated mode-number cutoff of $m \sim 6$. Inserting these numbers in Eq. (9), the growth rate as a function of the mode numbers is plotted in Fig 118.19.

After evolving through a linear regime, the growth of instabilities enters a nonlinear phase. In this phase, the unstable perturbations in the outward motion move into a region with reduced ambient pressure, resulting in reduced plasma density

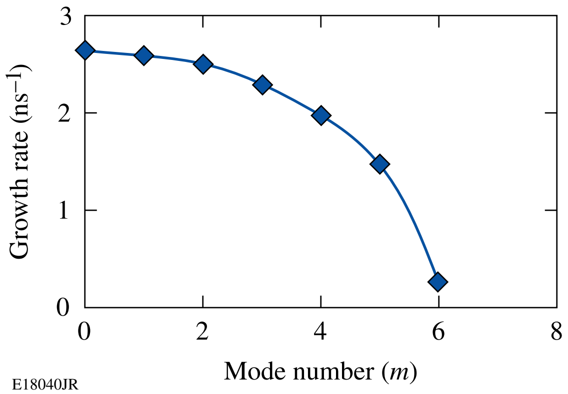

Figure 118.19
Growth rate determined using Eq. (3) is plotted as a function of the mode number for the plasma conditions discussed in this article, showing that the effects of stabilization will be cut off at $m \sim 6$.

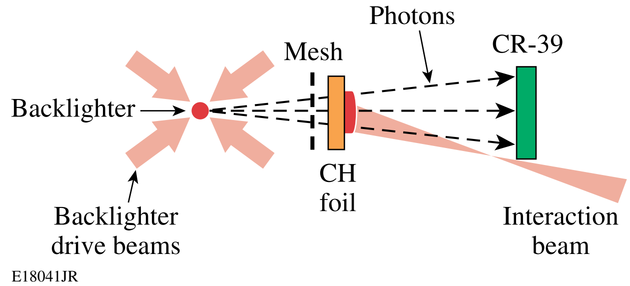

Figure 118.20
Schematic illustration of the experiment setup for face-on proton radiography. Distances from the backlighter are 1.3 cm for the mesh, 1.5 cm for the CH foil (5 μm thick), and 30 cm for the CR-39 detector.[6]

around the apex[4] and a reduced B field (causing a reduction of the field-line bending). These self-focusing effects tend to drive instabilities nonlinearly, leading to explosive growth.[17] Conversely, the nonlinear effects of inward motion of unstable perturbations tend to be stabilized, resulting from the field compression and plasma flow into the valleys.[17] The combined effects result in a finger-like structure: an explosive growth of outward instabilities and stabilized inward perturbations.[4]

Experiments

Pressure-driven, resistive instabilities were studied with monoenergetic proton radiography,[6–9,15,18] as shown schematically in Fig. 118.20, using a backlighter that produced pulsed protons at the discrete energy of 15 MeV (fusion products of the nuclear reaction D + ^{3}He $\longrightarrow \alpha$ + p, generated from D^{3}He-filled, thin-glass-shell implosions driven by 20 OMEGA laser beams[16]). Plasmas and B fields were generated through laser–plasma interactions on a plastic (CH) foil by a single laser beam (hereafter called the *interaction beam*) with a wavelength of 0.351 μm, linearly polarized, and incident at 23° from the normal direction. The 1-ns-long square laser pulse had an energy of ~400 J and a spot diameter of ~800 μm determined by phase plate SG4 (defined as 95% energy deposition),[19,20] resulting in a peak laser intensity of the order of 10^{14} W/cm. The nickel mesh used was 60 μm thick with 150-μm period and 75-μm holes.[6–9,15,18] Radiographs were recorded using CR-39 detectors.[21] The duration of each "exposure," determined by the emission time of the backlighter-produced protons, was ~130 ps. Since the backlighter-to-foil flight time for the protons was ~0.28 ns, an image representing the state of the field (at the foil at time t_a after the onset of the interaction beam) was made by starting this beam at time t_a + 0.28 ns after the mean backlighter-production time.

Data and Discussion

Face-on proton-radiograph images are shown in Fig. 118.21 (see Ref. 6). Each image is labeled with a time that represents the interval between the start of the interaction beam and the arrival of the backlighter protons and shows how the proton

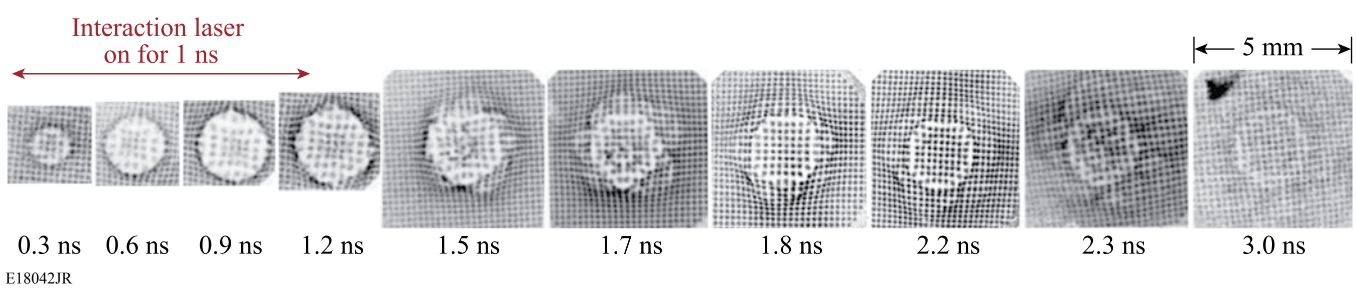

Figure 118.21
Measured face-on D^{3}He proton images showing the spatial structure and temporal evolution of B fields generated by laser–plasma interactions. Each image is labeled at the time between the arrival at the foil of the interaction beam and the arrival of the imaging protons. The images illustrate the transition from the 1-ns illumination period (with 2-D symmetric expansion of B fields), to a post-laser decay phase with 3-D structures emerging around the bubble edge and in the interior, as the expanding bubble cools and becomes increasingly resistive.

beamlets are deflected while passing through the B field that forms around the bubble.[22–24] The images show that while the laser beam is on ($t < 1.2$ ns), the field structure expands approximately in tandem with a hemispherical plasma bubble, maintaining 2-D cylindrical symmetry. Each image has a sharp circular ring where beamlets pile up after passing through the edges of the bubble, where the B fields are largest. This circle is a magnified image of the bubble edge because the angular deflection of each beamlet is proportional to $\int \mathbf{B} \times d\vec{\ell}$ (where $d\vec{\ell}$ is the differential pathlength along the proton trajectory) and $\mathbf{B} \times d\vec{\ell}$ points away from the bubble center.

When the laser turns off ($t > 1.2$ ns), the bubble continues to expand as the field decays and becomes distinctly asymmetric, indicating instability growth. This is contrary to the 2-D LASNEX simulations that cannot model 3-D asymmetries. It might be argued that the observation of a 3-D structure renders a comparison with the 2-D simulations irrelevant, but 3-D codes are not yet available and it is important to consider only the data at hand. (Work is currently underway on combining the 3-D hydrocode *HYDRA* with a field-generating package.[25]) Experimental measurements, such as those shown here, are important because they directly reveal previously unpredicted physical phenomena, indicate the fundamental importance of 3-D processes in certain regimes (such as in the decay phase), and provide invaluable information for benchmarking a true 3-D code. A rough estimate suggests that high-mode-number modes ($m \sim 3$ to 6) occur and are superimposed on the expanding plasma bubble. The time evolution of the imaging spatial structures clearly indicates that these modes are unstable and that their amplitudes grow continuously (Fig. 118.21). As described in the previous sections, the experimental conditions and plasma-bubble configuration satisfy the requirements for the appearance of pressure-driven resistive interchange instabilities: first, the bubble has unfavorable field curvature relative to the pressure gradient ($\boldsymbol{\kappa} \cdot \nabla P > 0$), in which field lines are concave toward the plasma and plasma pressure tends to expand outward; second, at these post-driven times, the fluid behavior near the bubble edge is dominated by field and resistive effects. Plasma resistivity significantly reduces the stabilization associated with field-line bending, making it possible for high-mode-number perturbations ($m > 1$) to destabilize and grow. As a consequence, these conditions result in the interchange of fields between the inside and outside of the bubble. Pure fluid instabilities such as the Widnall type[26] might be visible while the laser is on (when B fields have little impact on the plasma flow but are frozen in); there is no evidence that this is occurring.

The quantitative comparison of measured time evolution of rms deviations, defined as deviation of the outer-bubble boundary from the average radii, is given by:

$$\Delta r^2 = \frac{1}{N}\sum_{i}^{N}\left(r_i - \bar{r}\right)^2, \tag{13}$$

where N is the total number of the deviations, with calculated growth in the linear growth regime [Eq. (3)] given in Fig. 118.22. Experimental data are reasonably well reproduced using theoretical predictions and provide compelling evidence to support that they are caused by interchange instabilities. This agreement also suggests that the instability has dominant mode numbers $m \sim 3$ to 5. The measurement uncertainties are large, reflecting the uncertainties involved in determining the amplitudes of various perturbation modes. Finger-like structures associated with nonlinear growth do not appear. This suggests that the fields have dissipated sufficiently before the onset of nonlinear growth. This will be a topic for future study.

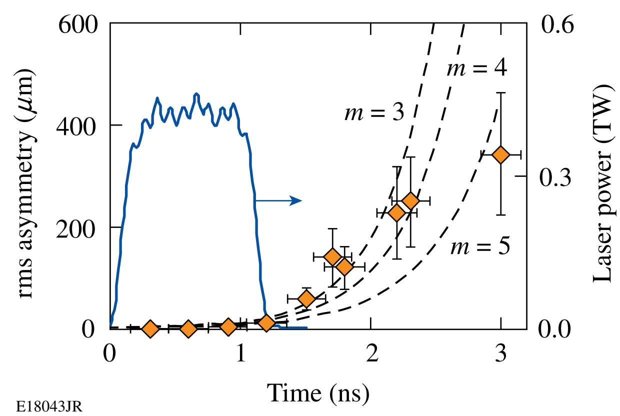

Figure 118.22
Measured time evolution of rms deviations of the outer-bubble boundary from the average radii (averaged azimuthally over angles from individual images) are shown to be reasonably consistent with the predicted growth of interchange instabilities. The solid curve is the time history of the laser intensity.

Summary

Pressure-driven, resistive magnetohydrodynamic interchange instabilities in laser-produced, high-energy-density plasmas have been studied with proton radiography. Unstable, high-mode-number perturbations ($m > 1$) occur around the expanding plasma bubble edge after the laser has turned off. The quantitative consistency between experimental data and theoretical prediction provides strong evidence for the occurrence and growth of interchange instabilities. A cutoff relation

for stabilization, $m > \sim\left[8\pi\beta\left(1 + D_{\mathrm{m}} k_{\perp}^{2}\, \gamma_{\max}^{-1}\right)\right]^{1/2}$, has been found in the linear growth regime and found to match the data. Experimental measurements are important for directly revealing, in a different context, previously unpredicted physical phenomena. They indicate the fundamental importance of 3-D processes in certain regimes and provide invaluable information for benchmarking 3-D code development.

ACKNOWLEDGMENT

The work was performed at the LLE National Laser User's Facility (NLUF), and was supported in part by US DOE (DE-FG52-07NA28059 and DE-FG52-06N826203), LLNL (B543881 and LDRD-ER 898988), LLE (414090-G), and the Fusion Science Center at the University of Rochester (412761-G).

REFERENCES

1. H. P. Furth, J. Killeen, and M. N. Rosenbluth, Phys. Fluids **6**, 459 (1963).
2. B. Coppi, Phys. Rev. Lett. **12**, 6 (1964).
3. J. P. Freidberg, *Ideal Magnetohydrodynamics* (Plenum Press, New York, 1987).
4. D. Biskamp, *Magnetic Reconnection in Plasmas*, Cambridge Monographs on Plasma Physics (Cambridge University Press, Cambridge, England, 2000).
5. R. P. Drake, *High-Energy-Density Physics: Fundamentals, Inertial Fusion, and Experimental Astrophysics, Shock Wave and High Pressure Phenomena* (Springer, Berlin, 2006).
6. C. K. Li, F. H. Séguin, J. A. Frenje, J. R. Rygg, R. D. Petrasso, R. P. J. Town, P. A. Amendt, S. P. Hatchett, O. L. Landen, A. J. Mackinnon, P. K. Patel, M. Tabak, J. P. Knauer, T. C. Sangster, and V. A. Smalyuk, Phys. Rev. Lett. **99**, 015001 (2007).
7. C. K. Li, F. H. Séguin, J. A. Frenje, J. R. Rygg, R. D. Petrasso, R. P. J. Town, P. A. Amendt, S. P. Hatchett, O. L. Landen, A. J. Mackinnon, P. K. Patel, V. A. Smalyuk, T. C. Sangster, and J. P. Knauer, Phys. Rev. Lett. **97**, 135003 (2006).
8. C. K. Li, F. H. Séguin, J. A. Frenje, J. R. Rygg, R. D. Petrasso, R. P. J. Town, O. L. Landen, J. P. Knauer, and V. A. Smalyuk, Phys. Rev. Lett. **99**, 055001 (2007).
9. C. K. Li, F. H. Séguin, J. R. Rygg, J. A. Frenje, M. Manuel, R. D. Petrasso, R. Betti, J. Delettrez, J. P. Knauer, F. Marshall, D. D. Meyerhofer, D. Shvarts, V. A. Smalyuk, C. Stoeckl, O. L. Landen, R. P. J. Town, C. A. Back, and J. D. Kilkenny, Phys. Rev. Lett. **100**, 225001 (2008).
10. L. Spitzer, *Physics of Fully Ionized Gases*, 2nd rev. ed., Interscience Tracts on Physics and Astronomy (Interscience, New York, 1962).
11. S. I. Braginskii, in *Reviews of Plasma Physics*, edited by Acad. M. A. Leontovich (Consultants Bureau, New York, 1965).
12. M. G. Haines, Phys. Rev. Lett. **78**, 254 (1997).
13. G. B. Zimmerman and W. L. Kruer, Comments Plasma Phys. Control. Fusion **2**, 51 (1975).
14. P. D. Nielsen and G. B. Zimmerman, Lawrence Livermore National Laboratory, Livermore, CA, Report UCRL-53123 (1981).
15. R. D. Petrasso, C. K. Li, F. H. Séguin, J. R. Rygg, J. A. Frenje, R. Betti, J. P. Knauer, D. D. Meyerhofer, P. A. Amendt, D. H. Froula, O. L. Landen, P. K. Patel, J. S. Ross, and R. P. J. Town, "Lorentz Mapping of Magnetic Fields in Hot, Dense Plasmas," to be published in Physical Review Letters.
16. J. M. Soures, R. L. McCrory, C. P. Verdon, A. Babushkin, R. E. Bahr, T. R. Boehly, R. Boni, D. K. Bradley, D. L. Brown, R. S. Craxton, J. A. Delettrez, W. R. Donaldson, R. Epstein, P. A. Jaanimagi, S. D. Jacobs, K. Kearney, R. L. Keck, J. H. Kelly, T. J. Kessler, R. L. Kremens, J. P. Knauer, S. A. Kumpan, S. A. Letzring, D. J. Lonobile, S. J. Loucks, L. D. Lund, F. J. Marshall, P. W. McKenty, D. D. Meyerhofer, S. F. B. Morse, A. Okishev, S. Papernov, G. Pien, W. Seka, R. Short, M. J. Shoup III, M. Skeldon, S. Skupsky, A. W. Schmid, D. J. Smith, S. Swales, M. Wittman, and B. Yaakobi, Phys. Plasmas **3**, 2108 (1996).
17. S. C. Cowley and M. Artun, Phys. Rep. **283**, 185 (1997).
18. C. K. Li, F. H. Séguin, J. A. Frenje, R. D. Petrasso, P. A. Amendt, R. P. J. Town, O. L. Landen, J. R. Rygg, R. Betti, J. P. Knauer, D. D. Meyerhofer, J. M. Soures, C. A. Back, J. D. Kilkenny, and A. Nikroo, Phys. Rev. Lett. **102**, 205001 (2009).
19. T. J. Kessler, Y. Lin, J. J. Armstrong, and B. Velazquez, in *Laser Coherence Control: Technology and Applications*, edited by H. T. Powell and T. J. Kessler (SPIE, Bellingham, WA, 1993), Vol. 1870, pp. 95–104.
20. D. D. Meyerhofer, J. A. Delettrez, R. Epstein, V. Yu. Glebov, V. N. Goncharov, R. L. Keck, R. L. McCrory, P. W. McKenty, F. J. Marshall, P. B. Radha, S. P. Regan, S. Roberts, W. Seka, S. Skupsky, V. A. Smalyuk, C. Sorce, C. Stoeckl, J. M. Soures, R. P. J. Town, B. Yaakobi, J. D. Zuegel, J. Frenje, C. K. Li, R. D. Petrasso, D. G. Hicks, F. H. Séguin, K. Fletcher, S. Padalino, C. Freeman, N. Izumi, R. Lerche, T. W. Phillips, and T. C. Sangster, Phys. Plasmas **8**, 2251 (2001).
21. F. H. Séguin, J. L. DeCiantis, J. A. Frenje, C. K. Li, J. R. Rygg, C. D. Chen, R. D. Petrasso, J. A. Delettrez, S. P. Regan, V. A. Smalyuk, V. Yu. Glebov, J. P. Knauer, F. J. Marshall, D. D. Meyerhofer, S. Roberts, T. C. Sangster, C. Stoeckl, K. Mikaelian, H. S. Park, H. F. Robey, and R. E. Tipton, Phys. Plasmas **13**, 082704 (2006).
22. The effects of scattering on proton deflection are minimum because of the negligible energy loss as the 15-MeV backlighting protons pass through the plasmas ($\rho L \sim 0.5$ mg/cm^2) (Refs. 23 and 24).
23. C. K. Li and R. D. Petrasso, Phys. Rev. Lett. **70**, 3059 (1993).
24. V. L. Highland, Nucl. Instrum. Methods **129**, 497 (1975).
25. M. M. Marinak *et al*., Phys. Plasmas **8**, 2275 (2001).
26. S. E. Widnall, D. B. Bliss, and C.-Y. Tsai, J. Fluid Mech. **66**, 35 (1974).